ACS OMEGA

Open Access

http://pubs.acs.org/journal/acsodf

Article

Thermoelectric Properties of $CrS_{2-x}Te_x$ (x: 0, 1, 2) Dichalcogenides Monolayers: First-Principles Study

Farva Tufail, Abdull Farooq, Altaf Ur Rahman,* Zeinhom M. El-Bahy, Gaber A. M. Mersal, M. Abdul,* Muhammad Nisar, and Bao Jingfu*

Cite This: *ACS Omega* 2024, 9, 23782−23792

Read Online

ACCESS | Metrics & More | Article Recommendations

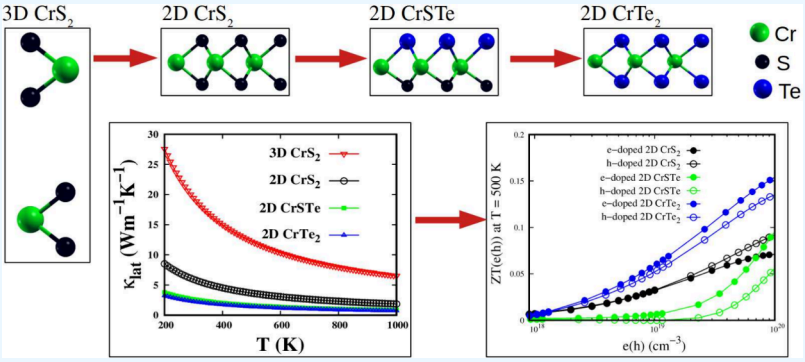

ABSTRACT: In this study, we conducted first-principles calculations interfaced with Boltzmann transport theory to examine the carrier-dependent thermoelectric properties of $CrS_{2-x}Te_x$ (x: 0, 1, 2) dichalcogenides monolayers. We conducted a systematic analysis of the structural, phonon band structures, elastic properties, electronic structures, and thermoelectric properties, of electron (e) and hole (h) doped $CrS_{2-x}Te_x$ (x: 0, 1, 2) dichalcogenides monolayers. The studied 2D TMDCs exhibit structural stability, as indicated by the negative formation energy. Additionally, the phonon band structures indicate no negative frequencies along any wave vector, confirming the dynamic stability of the $CrS_{2-x}Te_x$ monolayers. CrS_2 and $CrTe_2$ monolayers are semiconductors with direct bandgaps of 1.01 and 0.67 eV, respectively. A Janus CrSTe monolayer has a smaller bandgap of 0.21 eV. Temperatures range between 300 and 500 K, and concentrations of e(h) doped in the range of 1.0×10^{18}−1.0×10^{20} cm^{-3} are used to compute the thermoelectric transport coefficients. The low lattice thermal conductivity is predicted for the studied compounds, among which Janus CrSTe and $CrTe_2$ have the minimum value of $\kappa_{lat} \approx 1$ W/mK @ 700 K. The figure-of-merit ZT projected value at the optimal e(h) doping concentration for the CrS_2 monolayer is as high as 0.07 (0.09) at 500 K. Our findings demonstrate how to design improved thermoelectric materials suitable for various thermoelectric devices.

1. INTRODUCTION

Two-dimensional (2D) transition metal dichalcogenide (TMDC) materials have been garnering attention due to their tunable bandgap, large effective mass, and valley degeneracy. These properties make them promising for thermoelectric applications. 2D materials are becoming significantly helpful and have been the subject of many exciting research works which become suitable to specific use in our daily life.[1−6] This is due to the relatively simple layered crystal structure and their tunable structural, electronic, and thermoelectric properties.[5,7] Researchers in the twentieth century discovered a variety of 2D materials that are utilized in multiple applications to improve the standards of our daily life. Most of the uses established in the past century relied on nonrenewable energy sources. A unique kind of functional material with significant structural, electronic, optical, and thermoelectric properties is 2D materials. Transition metal dichalcogenides MX_2 is a big family of 2D materials that have more than 200 members. Numerous in-depth investigations on the configurations and architectures of 2D materials have been spurred by the materials' prospective applications in a range of industrial and technological fields.[8−12] Most 2D MX_2 materials share the same structure as MoS2, attracted the interest of researchers due to their low cost, ease of synthesis, and superior, tunable properties.[9] 2D layered semiconducting materials have found extensive use in various applications,

Received: February 23, 2024
Revised: April 15, 2024
Accepted: April 30, 2024
Published: May 21, 2024

and scientists are constantly exploring new efficient 2D materials that still need to be investigated. 2D materials have been used to build a wide range of technologies, including electronics, spintronics, solar cells, sensing devices, and LED (light-emitting diodes).[10] Researchers grew interested in these materials because of their use in the previously mentioned devices, and many of these materials with MX_2 hexagonal crystal structures have been found and reported.[5,7]

2D materials and their van der Waals (vdW) heterostructure with staggered band gaps at commensurate lattice constants have incident photon energy conversion predicted theoretically and demonstrated in laboratory.[1,2,4] The current energy crisis is due to the fact that energy consumption and demand are rising every day and that our natural fuel resources are limited. Hence, we need to reduce energy consumption and find alternative natural fuels. Thermoelectricity is the new field to generate electricity from the waste heat and can be considered a green energy source.[13−17] 2D materials used for thermoelectric application must have good thermoelectric performance evaluated through the dimensionless figure of merit (ZT).[18] Thermoelectricity based on the Seebeck effect and Peltier effect has piqued academic curiosity for a long time. Theoretical and experimental efforts are being considered to improve the thermoelectric performance of materials.[17] The performance of thermoelectric generators is calculated by the figure of merit (ZT) using the equation:

$$ZT = \frac{\sigma S^2}{\kappa_e + \kappa_{lat}} T \quad (1)$$

in which σ, S, T, κ_e, and κ_{lat} are the electronic conductivity, Seebeck coefficient, working temperature, and electronic and lattice thermal conductivities, respectively. Investigation for a material to be employed in thermoelectric devices is in progress, and it must have $Z > 1$.[4] The following methods can enhance the ZT of thermoelectric materials: (i) clamping the phonon conduction, which will result in low lattice thermal conductivity, and (ii) enhancing electronic conductivity and Seebeck coefficient and reduced electronic thermal conductivity. Currently, few 2D materials have high ZT > 3, and the researchers are consistently trying to enhance ZT because reducing dimensionality, which terminated the electronic motion in the vertical direction of the plane of material.[17,19] Among 2D materials, transition metal dichalcogenides (TMDCs) is the largest family of 2D materials that have been got considerable attention in recent years in the field of thermoelectricity.[20,21] Thermoelectric properties of TMDCs such as MoS_2, $MoSe_2$, $MoTe_2$, WS_2, WSe_2, and WTe_2 have been studied for their possible thermoelectric applications.[22,23]

Furthermore, when compared to the bulk counterpart of the 2D materials, the monolayer has a direct bandgap, which enhances the electronic conductivity and Seebeck coefficient, which results in a large ZT.[4,24] Material scientists are actively involved in enhancing the efficiency of materials used in thermoelectric devices by improving ZT. Usually, ZT is greater than three of the conventional thermoelectric materials used in thermoelectric devices.[25] TMDCs have electronic dispersion in which the energy of electrons does not vary significantly with wave vector "k", i.e., the bands have small curvature, resulting in a higher effective mass. As we know, the thermopower strongly depends on the carrier-effective mass, so the TMDCs monolayer exhibits high thermoelectric performance compared to the bulk phase, which is attributed to the direct and quantum confinement of electron motion in a 2D plane. Besides this, 2D materials have low electronic thermal conductivity and phonon conductivity ($\kappa_{tot} = \kappa_e + \kappa_{lat}$), which is essential to enhance ZT.

There are various strategies to enhance the thermoelectric performance of the TMDCs monolayer, including functionalization, substitutional doping, and external field. For example, researchers have proposed 2D materials and 2D van der Waals heterostructures for thermoelectric applications.[26,27] Identifying a promising material with a high thermoelectric efficiency is still a challenge despite the various attempts to predict such materials through both theoretical and experimental means. This article focuses on the electronic and thermoelectric properties of CrS_2, CrSTe, and $CrTe_2$ monolayers [see Figure 1(a−c)]. Thermoelectric properties will be investigated as a function of electron (e) and hole (h) doping concentrations and working temperatures. The review also considers the impact of the Janus effect on the electronic and transport properties of the pristine monolayers.

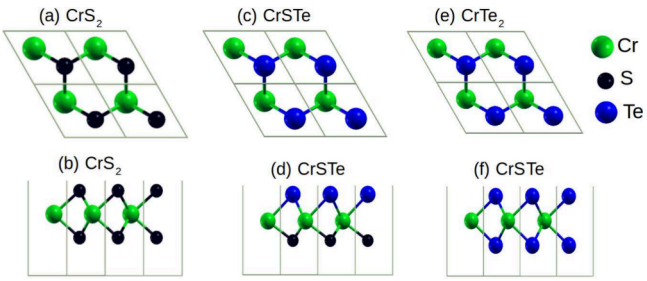

Figure 1. Schematic top and side view representation of the hexagonal crystal structure (a, b) 1H-CrS_2, (c, d) 1H-CrSTe, and (e, f) 1H-$CrTe_2$ monolayers. The Cr, S, and Te atoms are represented by green, black, and blue spheres, respectively.

2. COMPUTATIONAL METHODOLOGY

First-principles calculations within the framework of DFT[28] were performed using QUANTUM ESPRESSO package.[29] The generalized gradient approximation (GGA) with the Perdew−Burke−Ernzerhof (PBE) parametrization was used to calculate the exchange-correlation energy and potential.[30] The ultra-pseudopotentials were parametrized using the recipe of Rappe, Rabe, Kaziras, and Joannopouls.[31] The valence electrons were treated fully relativistically for the spin−orbit coupling (SOC) calculations. A pseudopotential developed by Dal Corso within the PBE form was utilized, which considered only the valence electrons for physical and chemical properties. For example the valence electrons are $4s^1 3d^5$ for Cr, $3s^2 3p^4$ for S, and $4s^2 4p^4$ for Se atoms. These pseudopotentials are freely available on the QUANTUM ESPRESSO webpage: https://www.quantum-espresso.org/pseudopotentials/. We employed the following freely available pseudopotentials from the QUANTUM ESPRESSO webpage: *Cr.pbe-spn-rrkjus-psl.1.0.0.UPF*, *S.pbe-n-rrkjus-psl.1.0.0.UPF*, and *Se.pbe-n-rrkjus-psl.1.0.0.UPF* for Cr, S, and Se atoms, respectively.

The electronic wave functions were expanded in a plane wave basis set with an energy cutoff of 60 Ry and a charge density cutoff of 240 Ry. To sample the first Brillouin zone (BZ), the Monkhorst−Pack scheme is used[32] with a 12 × 12 × 1 mesh for geometry optimization. A denser 22 × 22 × 1 mesh was used to calculate the electronic properties. For the geometry optimization, the fractional coordinates of all atoms

https://doi.org/10.1021/acsomega.4c01767
ACS Omega 2024, 9, 23782−23792

Table 1. Optimized Lattice Constant a, Bond Lengths Cr−S (denoted as b_{Cr-S})b and Cr−Te (b_{Cr-Te}), Thickness of the Monolayer (Δh), Bonding Angle Cr−X−Cr, E_f, and Direct and Indirect Bandgap of All the Investigated Compounds

compound	a (Å)	b_{Cr-S} (Å)	b_{Cr-Te} (Å)	Δh (Å)	θ(XCrX) (deg)	E_f (eV)	E_g(K−K) (eV)	E_g(Γ−K) (meV)
CrS_2	3.04 (3.05)[35]	2.32		2.93	87.17	−3.23	1.01	1.34
CrSTe	3.27 (3.32)[36]	2.42	2.75	3.16	84.30	−2.43	0.83	0.31
$CrTe_2$	3.47		2.13	3.41	91.26	−2.05	0.67	0.95
	(3.31)[35]	(2.36)[37]	(2.12)[37]					(0.95),[37] (0.89)[35]

present in the unit cell were allowed to relax until the Hellmann−Feynman forces were lower than 0.002 Ry/Bohr. To ensure the thermodynamic stability, we estimated the formation energy, which is defined as

$$E_f = \{E_{tot[CrSTe]} - E_{tot[Cr]} - E_{tot[S]} - E_{tot[Te]}\} \quad (2)$$

where $E_{tot[CrSTe}$ represents the ground state energy of $CrSTe_3$ compounds and $E_{tot[Cr]}$, $E_{tot[S]}$, and $E_{tot[Te]}$ represent the optimized total energy per Cr, S, and Te atoms in the most stable phase, respectively. The most stable phase of the Cr atom is its natural phase (BCC: body-centered cubic), which is made of two atoms per primitive unit cell.[33] For the S atom, the total energy is calculated by considering the hexagonal phase of the (S_6) molecule,[34] which is utilized to determine the chemical potential of halogen. We also calculated the phonon spectrum and lattice thermal conductivity, which will be explained in the next separate section.

3. RESULTS AND DISCUSSION

3.1. Structural Properties of $CrS_{2-x}Te_x$ Monolayers. The ball and stick model of the 1H-$CrS_{2-x}Te_x$ hexagonal crystal with space group $P3m1$ in the 1H phase is depicted in Figure 1(a−f). Figure 1(a,b) represents the schematic top and side views of the CrS_2 monolayer. Six chalcogen atoms surround the Cr atom and form a hexagonal crystal structure. TMDCs are layered structures having three atomic layers stacked together with covalent bonding. Figure 1(a,b) depicts the conventional unit cell of the CrS_2 monolayer, where the Cr atom is covalently bonded with the chalcogen atoms. We first optimized the ground state properties of the CrS_2 monolayer, and the results are listed in Table 1 and are compared with previously reported results. Once we confirmed the accuracy of our calculations, we further considered Janus CrSTe and $CrTe_2$ monolayers for our investigation. Functionalizing the CrS_2 monolayer with 50% concentration of the Te atoms, a Janus CrSTe monolayer is formed as shown in Figure 1(c,d). The Te atom is substituted at the S-sites in the CrS_2 monolayer. Figure 1(e,f) shows the top and side views of the $CrTe_2$ monolayer. Theoretically, calculated total energies as a function of volume are fitted to the Murnaghan equation of state to obtain equilibrium lattice constant.[38]

For the lattice constant optimization, we used the smallest unit cell of the $CrS_{2-x}Te_x$ monolayer, which contains three atoms per unit cell. The GGA+PBE optimized lattice constants are listed in Table 1. The lattice parameter and electronic bandgap are strongly affected by the type and concentration of chalcogen atoms present in the $CrS_{2-x}Te_x$ monolayer. The isolated Cr atoms are magnetic in nature, and also Cr-X bonds formed in the 1H-$CrS_{2-x}Te_x$ monolayer induce strong anharmonicity, which will result in low phonon conduction, which is essential for novel thermoelectric materials. The ground state lattice parameter are 3.04, 3.27, and 3.47 Å for CrS_2, CrSTe, and $CrTe_2$ monolayers, respectively [see Table 1]. The calculated bond length b_{Cr-S} slightly increased because the S atom was replaced with the Te atom. By increasing the concentration of the Te atom, the b_{Cr-Te} got enhanced. As a result, the thickness Δz of the monolayer increased (see Table 1). The previously reported lattice constants are 2.99,[39] 3.47,[40] and 3.31 Å[35] for CrS_2, CrSTe, and $CrTe_2$ monolayers, respectively. These values are slightly different from our reported values. This is due to the different scheme of pseudopotentials methods.[41]

The values enclosed in parentheses are associated with the corresponding compounds. For instance, in the initial row of Table 1, we compare the computed lattice constant of CrS2 monolayers with the previously reported values, which are listed in the small brackets. Table 1 shows that as we substitute the S atom with Te atoms in the CrS_2 monolayer, the thickness of the monolayer increases due to the electronegativity (EN) difference between the S and Te atoms. The EN of the Te atom is 2.1, slightly less than the EN (2.58) of the S atom. Formation energy is the change in energy when a materials is formed from its constituent atoms in the their natural phase. For example, the negative sign of the calculated formation energy indicates that when the Cr (BCC phase) and S (S_6 phase) is used as a source, the CrS_2 monolayer formation reaction is exothermic, so negative formation energy represents thermodynamic stability of the compounds. To check structural stability, formation energy (E_f) is calculated at the equilibrium lattice constant. The obtained E_f values are −3.23, −2.43, and −2.05 eV, for CrS_2, CrSTe, and $CrTe_2$ monolayers, respectively. Experimentally, the compound with negative formation energy will be easily formed in exothermic reaction.[42] The CrS_2 has a more negative formation energy, which means that it is more stable compared to the other investigated compounds.

The trend followed by the formation energies of the investigated compound is consistent with the thermodynamic stability, which decreases as the lattice constant increases. This is also consistent with electronegativity differences between the constituent elements, i.e., the lattice increases with an increase in electronegativity difference between Cr-X atoms present in the compound. Next, to check the dynamic stability, we calculated the phonon dispersion of all the compounds under consideration.

3.2. Phonon Band Structure and Lattice Thermal Conductivity. To calculate the second-order interatomic force constants (IFCs-2) harmonic terms, PHONOPY code[43] was used by employing the finite displacement method. The graph in Figure 2a−c displays the phonon band structure along the high symmetry points that form a closed path Γ−M−K−Γ in the first Brillouin zone. It is noteworthy that there are no negative frequencies at any vector for the phonon band structure, indicating that the compounds being studied are kinetically stable. The mechanical stability of $CrS_{2-x}Te_x$ hexagonal crystal structures can be confirmed by calculating the two independent elastic constants C_{11} and C_{12} define as

https://doi.org/10.1021/acsomega.4c01767
ACS Omega 2024, 9, 23782−23792

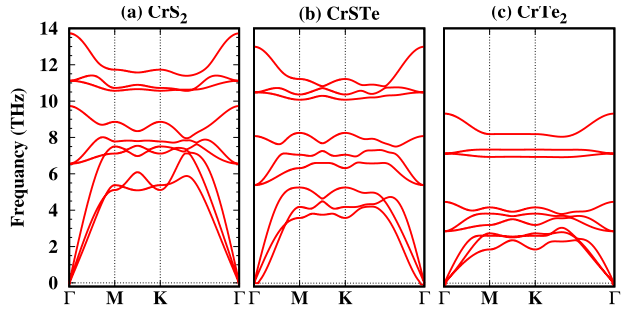

Figure 2. Phonon band structure of (a) pristine CrS_2 monolayer, (b) Janus CrSTe monolayer, and (c) pristine $CrTe_2$ monolayer at equilibrium lattice constant.

$$C_{11} = C_{11} = \frac{1}{A_o}\frac{\partial E^2}{\partial \varepsilon_{11}^2} \quad \text{and} \quad C_{12} = \frac{1}{A_o}\frac{\partial E^2}{\partial \varepsilon_{11}\partial \varepsilon_{12}} \tag{3}$$

Here, E is the total energy of a supercell 2 × 1 × 1 (rectangular unit cell) used for the calculations, and A_o is the area of the rectangular unit cell at ground state lattice constant. The calculated elastic constants are listed in Table 2, which

Table 2. Calculated Elastic Constants C_{ij}, Shear Modulus (G), Young's Modulus (Y), and Poisson's Ratio (ν) for CrS_2, CrSTe, and $CrTe_2$ Monolayers[a]

compound	$C_{11} = C_{22}$	C_{12}	G	Y	ν
CrS_2	112.45	29.76	21.30	29.23	0.26
CrSTe	97.56	22.45	18.85	21.98	0.23
$CrTe_2$	83.76	19.83	16.75	19.36	0.23

[a]The elastic constants are measured in units of Newton per meter. G, Y, and ν are dimensionless.

satisfy the Born criteria $C_{11} > 0$, $C_{11} - C_{12} > 0$, and $C_{66} > 0$ of mechanical stability for hexagonal crystal structures, which ensure that 2H $CrS_{2-x}Te_x$ monolayers are mechanically stable. Table 2 listed the Young's modulus of CrS_2 and CrSTe monolayers, which shows that Y of CrSTe is slightly smaller than that of the CrS_2 monolayer, which is the indication of more flexible behavior of the CrSTe monolayer than the CrS_2 monolayer. This occurs due to the weak Cr−Te bond length compared with the Cr−S bond length, as shown in Table 1.

However, the phonon thermal conductivity plays a vital role in calculating the thermoelectric characteristics of a material. Based on the supercell approach using the finite displacement method, different PW inputs are created, among which atomic positions are displaced by amount 0.03 Å. Using PHONO3PY code,[43,44] the third-order interatomic force constant (IFCs-3) is obtained by using a 3 × 3 × 1 supercell with a k-point mesh of 5 × 5 × 1. Using IFCs-2 together with IFCs-3, the lattice thermal conductivities are computed by sampling the reciprocal spaces of primitive unit cells using 20 × 20 × 1 meshes. The PHONO3PY code was used to solve the BTE with a single-mode relaxation time approximation and calculate the lattice thermal conductivity.

The lattice thermal conductivity (κ_{lat}) of CrS_2, CrSTe, and $CrTe_2$ monolayers has been calculated at room temperature and at higher temperatures (Figure 3). At room temperature, κ_{lat} values for CrS_2, CrSTe, and $CrTe_2$ are 5.92, 2.64, and 2.28 Wm^{-1}/K, respectively. At 400 K, κ_{lat} values are 4.53, 2.06, and 1.76 Wm^{-1}/K for CrS_2, CrSTe, and $CrTe_2$ monolayers, respectively. At 500 K, the κ_{lat} values are 3.67, 1.66, and 1.41

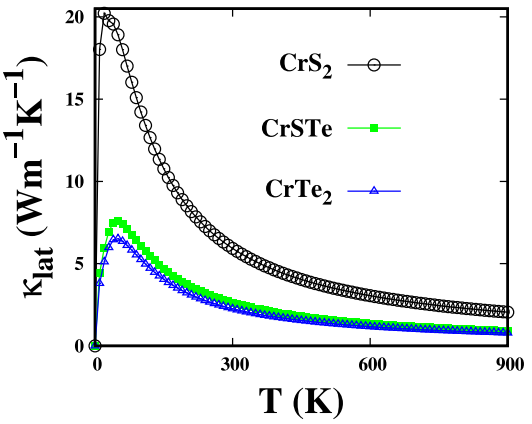

Figure 3. Lattice thermal conductivity κ_{lat} as a function of temperature. The black empty circle, green filled square, and blue triangular line points indicates the κ_{lat} calculated CrS_2, CrSTe, and $CrTe_2$ monolayers, respectively.

Wm^{-1}/K for CrS_2, CrSTe, and $CrTe_2$ monolayers, respectively. The lattice thermal conductivity decreases with an increase in temperature and reaches a minimum value at 900 K and is given by 2.09, 0.99, and 0.80 Wm^{-1}/K for CrS_2, CrSTe, and $CrTe_2$ monolayers, respectively.

3.3. Electronic Structure of $CrS_{2-x}Te_x$ Monolayers. To explore the electronic properties of $CrS_{2-x}Te_x$ monolayers, the electronic band structure is calculated by using the GGA+PBE method as shown in Figure 4(a−c). The estimated direct band

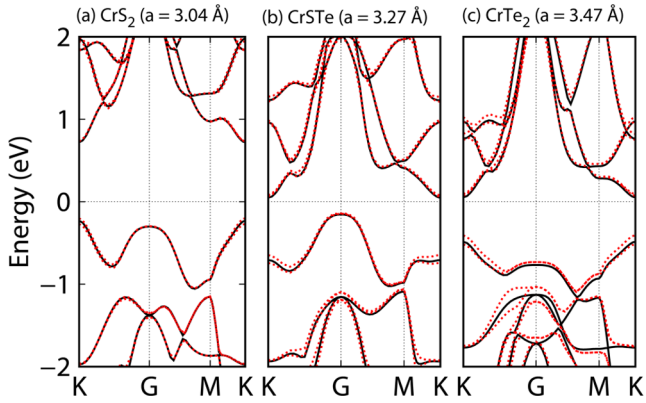

Figure 4. Black solid line (without SOC) and red dashed line (with SOC) represent the calculated electronic band structures of (a) CrS_2 [E_g = 1.01 eV (K−K)], (b) Janus CrSTe [E_g = 0.31 eV (Γ−K)], and (c) $CrTe_2$ [E_g = 0.67 eV (K−K)] dichalcogenides monolayers. The horizontal black line represents the Fermi energy level.

gaps are 1.01 (K−K), 0.37 (Γ−K), and 0.67 (K−K) for CrS_2, CrSTe, and $CrTe_2$ monolayers, respectively. Meanwhile, considering the disadvantages of the GGA+PBE functional in underestimating the bandgap for semiconductors, the hybrid functional HSE06 is used in this work to estimate the electronic bandgap accurately. We only used self-consistent field HSE calculations to estimate the HSE bandgap values. The HSE06 calculated band gap values are 1.52, 1.45, and 1.07 eV for CrS_2, CrSTe, and $CrTe_2$ monolayers, respectively. The previously reported HSE06 bandgap values are 1.48, 1.34, and 0.89 for CrS_2, CrSTe and $CrTe_2$ monolayers, respectively.[39,45] 2D materials were demonstrated to exhibit tunable bandgaps achieved via increasing the layer thickness, strain engineering,

https://doi.org/10.1021/acsomega.4c01767
ACS Omega 2024, 9, 23782−23792

chemical bonding, interface effect, and substitutional doping.[46] For example, previously, it was demonstrated for 2D materials that due to applied compressive (tensile) biaxial strain, a transition from indirect (direct) to direct (indirect) bandgap occurred,[6,47] so when we replace the S atom with the Te-atom in the case of a Janus CrSTe monolayer, it induces an interface effect and strain effect, due to which direct to indirect bandgap transition occurs.

In addition, the electronic band structures of CrS_2, CrSTe, and $CrTe_2$ monolayers are calculated at the equilibrium lattice constant with and without spin−orbit coupling, as shown in Figure 4(a−c). However, we found no significant spin-splitting in these compounds. The magnitude of the SOC at the K-point is approximately 90 meV in all of these compounds. In the next section, we will discuss the thermoelectric response of the $CrS_{2-x}Te_x$ monolayers. With an increasing demand for clean energy, researchers in the thermoelectric field have been exploring the use of 2D materials in thermoelectric generators. The conversion of vast amounts of heat into useful energy has long been considered a promising renewable energy source. Several records for the highest ZT have been broken in recent years due to novel materials, new processing methods, and new mechanisms.[48,49] Khazaei et al.,[42] calculated a very high Seebeck (S) value for the Ti_2CO_2 and $Sc_2C(OH)_2$ compounds. In our previous work,[50,51] we presented a computational method for thermoelectric calculations.

We calculated the electron charge density displayed in Figure 5(a−c) in order to support our theory regarding the electronic band structure. The electron charge density indicates that the majority of the charge density is concentrated around the Cr atoms, while there is some charge localization around the S/Te atoms. This significant charge localization corresponds to the flat band in the electronic band structure with a small band curvature. As illustrated in the electronic band structure [refer to Figure 4(a-c)], the CrS_2 has a smaller (larger) band curvature, which leads to the large (small) effective mass of the hole (electron). Consequently, the hole has a larger Seebeck coefficient. As we know, a larger Seebeck coefficient corresponds to a higher thermopower factor, PF, which will ultimately result in a higher value of the figure-of-merit ZT.

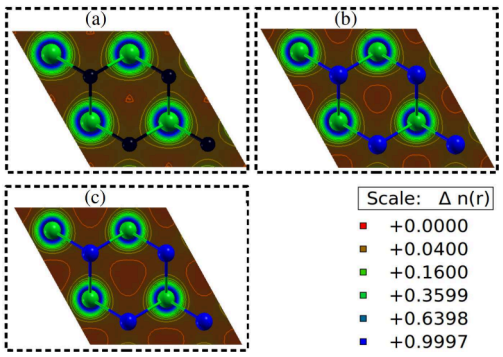

Figure 5. Calculated electronic charge density along (001) surface is computed for 2D $CrS_{2-x}Te_x$ monolayers; (a) CrS_2, (b) Janus CrSTe, and (c) $CrTe_2$. The green, black, and blue sphere represents the Cr, S, and Te atoms, respectively.

3.4. Thermoelectric Properties of $CrS_{2-x}Te_x$ Monolayers. Scientists have traditionally used the semiclassical Boltzmann equation to calculate the thermoelectric properties of different compounds.[4] This equation is based on the constant relaxation time approximation, which assumes that the material's scattering time remains unchanged with energy. This method has been effective in predicting the thermoelectric behavior of various 2D and 3D materials in the past, as evidenced by previous research studies.[51−54] This has been examined both experimentally and conceptually, and the results are highly accurate.[51,53] In the BoltzTrap code, constant relaxation time ($\tau = 10^{14}$) is used in the computations for the thermoelectric properties.[55] In a recent study, the relaxation time ($\tau = 10^{14}$) was used to determine the thermoelectric properties of the 2D $CrS_{2-x}Te_x$ monolayer.

In the 2D $CrS_{2-x}Te_x$ monolayer, unlocalized charges, electron and hole, were added to the host to study the effects on thermoelectric properties. By setting the chemical potential equal to the Fermi energy, an estimate of the thermoelectric characteristics as a function of temperature and electron (hole) (denoted as the e(h)) doping concentration for $CrS_{2-x}Te_x$ monolayers is derived. For $CrS_{2-x}Te_x$ monolayers, the electronic conductivity is represented by $\sigma(T, \text{e(h)})$ in Figure 6(a−c). The electronic conductivity $\sigma(T, \text{e(h)})$ is plotted against the T and e(h) doping concentrations. Because the Fermi level lies approximately 0.60 eV below the CBM, Figure 6(a) illustrates that the electrical conductivity ($\sigma(T, \text{e(h)})$ does not change considerably with varying temperatures. The conductivity of a material, represented by $\sigma(T, \text{e})$, remains unchanged when the temperature is increased due to thermal excitation. This suggests that the electrons in the material did not receive enough energy to move into the conduction band

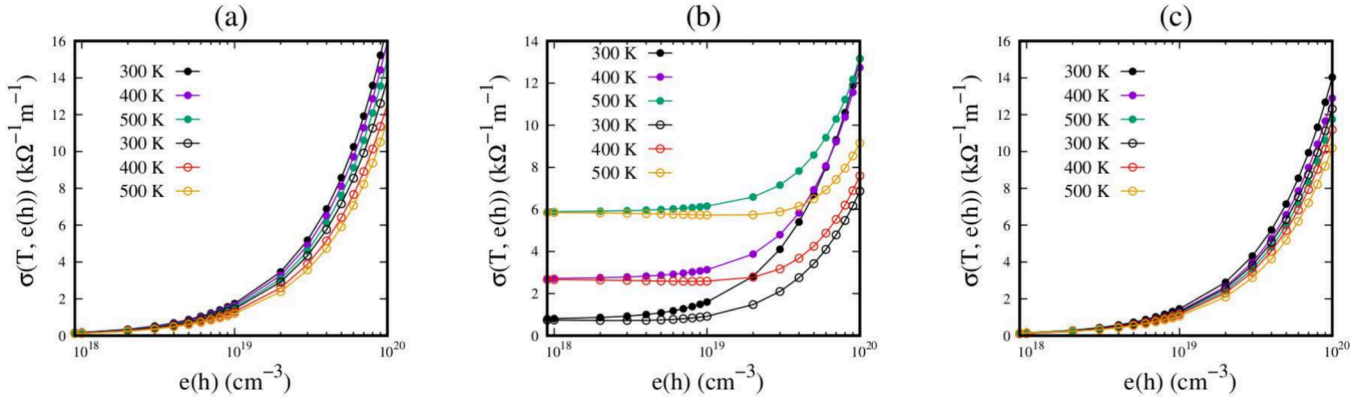

Figure 6. Electronic conductivity ($\sigma(T, \text{e(h)})$ of $CrS_{2-x}Te_x$ monolayers as a function of temperature and electron (hole) doping concentrations e(h). (a) $\sigma(T, \text{e(h)})$ of CrS_2, (b) $\sigma(T, \text{e(h)})$ of a Janus CrSTe, and (c) $\sigma(T, \text{e(h)})$ of $CrTe_2$ monolayers.

https://doi.org/10.1021/acsomega.4c01767
ACS Omega 2024, 9, 23782−23792

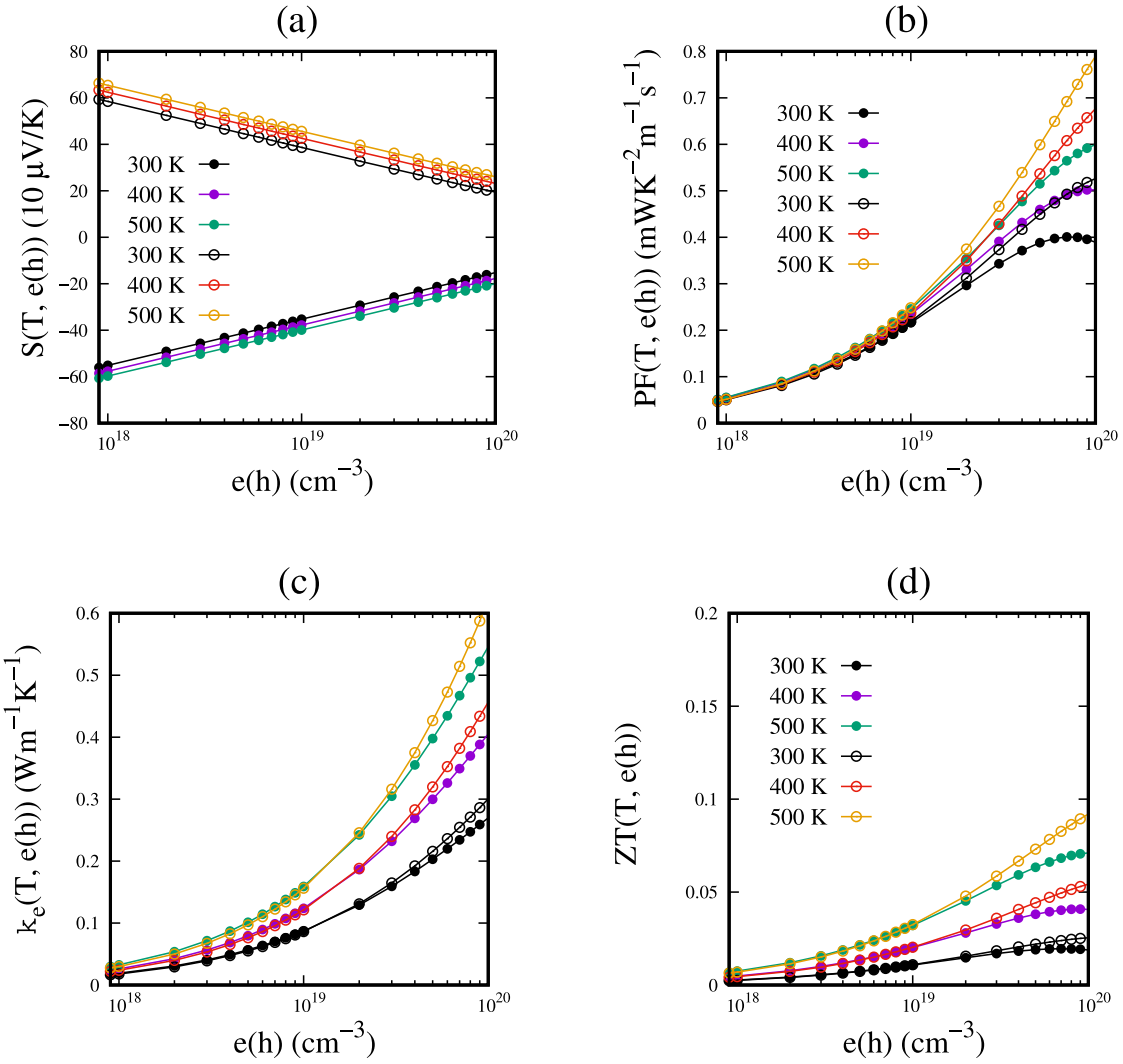

Figure 7. Thermoelectric characteristics of CrS_2 monolayers as a function of temperature and e(h) doping concentrations. (a) Seebeck coefficient (S), (b) power-factor (PF), (c) electronic (hole) thermal conductivity (κ_e), and (d) figure-of-merit (ZT).

and begin conducting. However, the conductivity of the material due to holes, represented by $\sigma(T, \text{h})$, shows a slight variation in response to changes in the temperature. This is because the hole will readily begin conduction as temperature changes because the Fermi level is near the valence band. It is demonstrated that as the concentration of e(h) doping rises logarithmically, $\sigma(T, \text{e(h)})$ increases in a nonlinear manner. The in-plane $\sigma(T, \text{e(h)})$ of the CrS_2 and $CrTe_2$ monolayers is shown in Figure 6(a, c), which suggests that it is not considerably affected by the temperature. On the other hand, $\sigma(T, \text{e(h)})$ of a Janus CrSTe monolayer is shown in Figure 6(b), which shows a notable increase when the temperature is raised from 300 to 500 K. Additionally, a considerable change in $\sigma(T, \text{e(h)})$ is projected as the doping concentration varies. Thus, the concentration of e(h) doping significantly impacts thermoelectric parameter optimization. This is why we considered an e(h) range of 1.0×10^{18}−1.0×10^{20} cm^{-3}.

The electronic band structures presented in Figure 4(a−c) indicate that the electron above the Fermi level in the conduction band follows a parabolic dispersion K−Γ spanning over the energy range of 0.10−1.0 eV in $CrS_{2-x}Te_x$ monolayers. In contrast, holes followed a flat dispersion at Γ−M in the valence band. As we know, effective mass (m^*) is inversely proportional to band curvature, i.e., a flat band centered at Γ point in the valence band means the band curvature is small, which results in a large effective mass of the carriers in cases where an electron or hole follows parabolic energy-momentum ($E \approx k^2$) dispersion. A flat band results in a heavy hole compared to electrons. The heavy holes give a large value of the Seebeck coefficient (S) in the case of h-type doping in $CrS_{2-x}Te_x$, as shown in Figure 7(a) and Figure 9(a), respectively. For example, at optimal hole doping concentration 1.0×10^{19} cm^{-3} and at room temperature, the compound values of Seebeck coefficients are 442, 350, and 597 μV/K for CrS_2, CrSTe, and $CrTe_2$ monolayers, respectively. The values of the Seebeck coefficient are larger than the absolute value of materials used for thermoelectric applications.[49] For example, using the two-probe method at room temperature, thermoelectric measurement was carried out, and the absolute value of Seebeck coefficient 389 μV/K was recorded for a few layers WS_2 material.[56] Such type of efficient thermoelectric material shows an excellent electronic mobility of 16.5 cm^2/(V s) and validates the potential of 2D TMDCs in thermoelectricity generation.[56] The trend is also consistent with previously reported in-plane Seebeck coefficient for two-dimensional ZrS_2 and ZrSSe monolayers.[20] It is also found that

https://doi.org/10.1021/acsomega.4c01767
ACS Omega 2024, 9, 23782−23792

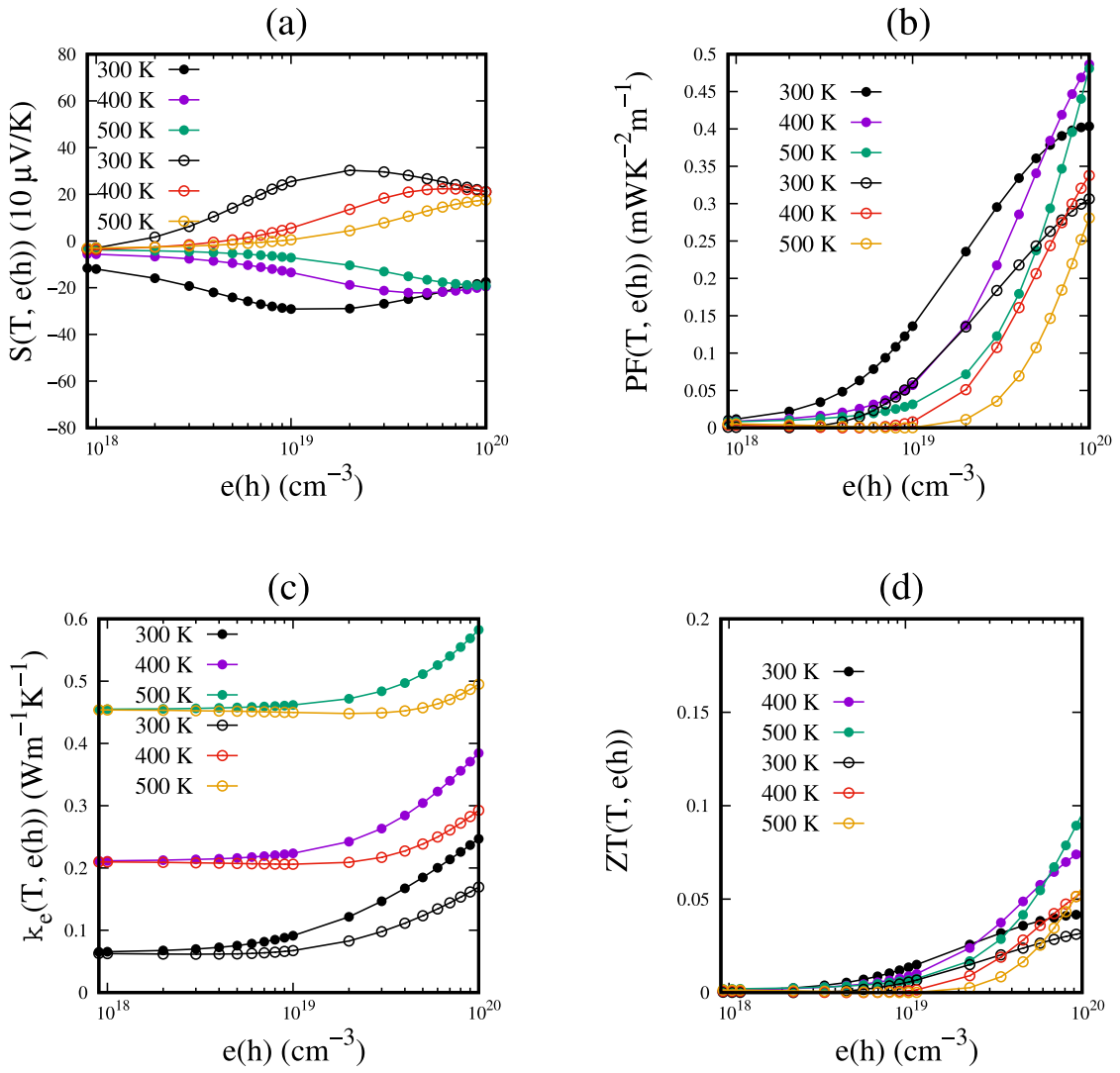

Figure 8. Thermoelectric characteristics of Janus CrSTe monolayers as a function of temperature and e(h) doping concentrations. (a) Seebeck coefficient (S), (b) power-factor (PF), (c) electronic (hole) thermal conductivity (κ_e/τ), and (d) figure-of-merit (ZT).

the Seebeck coefficient in the case of n-type doped $CrS_{2-x}Te_x$ monolayers followed pretty much the same behavior and has a lower value than p-type doped $CrS_{2-x}Te_x$ monolayers. However, the Seebeck coefficient for the studied compounds decreases with an increase in the temperature, as shown in Figure 7(a) and Figure 9(a).

Generally speaking, a higher ZT may be possible where the PF is high and total thermal conductivity is low. It has been previously reported that 2D $ZrSe_2$ and $HfSe_2$ monolayers have low lattice thermal conductivity and a promising figure of merit.[57] Among 2D TMDCs, MoS_2 is considered a promising candidate material for thermoelectricity because it has a high power factor since the discovery of 2D materials.[58] Figure 7(b) represents the PF of the CrS_2 monolayer; the calculated PF increases correspondingly with increasing e(h) doping concentrations and temperature. For p-type doped CrS_2 monolayer at doping concentration level 1.0×10^{20} cm^{-3}, the calculated values of PF are 0.80×10^{-3}, 0.67×10^{-3}, and 0.50×10^{-3} W/Km for 300, 400, an]d 500 K, respectively. For bilayer MoS_2 at high carrier concentrations, the experimentally observed value of PF is 8.5×10^{-3} W/Km.[58] The magnitude of PF is expected to increase up to the optimal doping concentration level; after that, PF starts decreasing even for further high doping concentrations as the increasing electrical conductivity [Figure 6(a)] is offset by the decreasing Seebeck coefficient [Figure 7(a)].

The computed band structure shows that the hole dispersion at the K point proliferates in the valence band, resulting in higher electrical conductivity compared to Janus CrSTe and pristine $CrTe_2$ monolayers. The high electrical conductivity and high Seebeck coefficient result in good thermoelectric characterization of CrS_2 monolayers instead of Janus CrSTe [Figure 8(a,b)] and pristine $CrTe_2$ monolayers [see Figure 9(a,b)]. Figure 4(b) shows the flat band dispersion for holes in the valence band and the parabolic dispersion for electrons in the conduction band. Due to this, hole conductivity grows slowly compared to electronic conductivity, as shown in Figure 7(b). Due to this reason, the PF calculated for a Janus CrsTe monolayer was suppressed in magnitude, as shown in Figure 8(b). For n-type doped CrSTe monolayer at doping concentration level 1.0×10^{20} cm^{-3}, the calculated values of PF are 0.41×10^{-3}, 0.48×10^{-3}, and 0.47×10^{-3} W/Km for 300, 400, and 500 K, respectively. Similarly, in the case of $CrTe_2$ monolayer, at a doping concentration level of 1.0×10^{20}

https://doi.org/10.1021/acsomega.4c01767
ACS Omega 2024, 9, 23782−23792

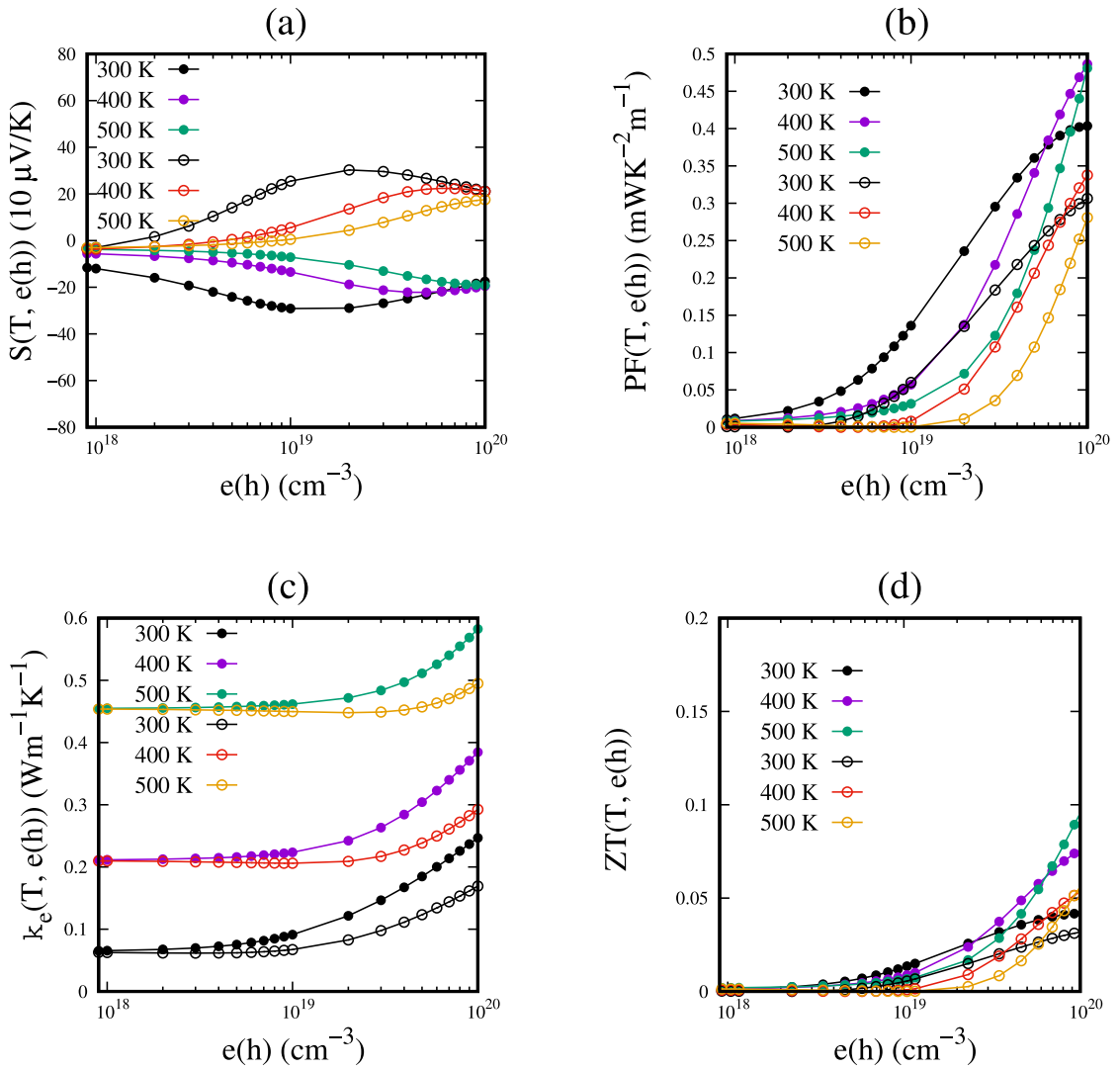

Figure 9. Thermoelectric characteristics of $CrTe_2$ monolayers as a function of temperature and e(h) doping concentrations. (a) Seebeck coefficient (S), (b) power-factor (PF), (c) electronic (hole) thermal conductivity (κ_e/τ), and (d) figure-of-merit (ZT).

cm^{-3}, the calculated values of PF are 0.61×10^{-3}, 0.48×10^{-3}, and 0.37×10^{-3} W/Km for 300, 400, and 500 K, respectively.

Electron-generated heat flow in a material is called electronic thermal conductivity, represented by the symbol κ_e, and similarly, hole thermal conductivity is represented by κ_h. The sum of the heat conduction from phonons (κ_{ph}) and the electronic or ionic thermal conductivity from electron (hole) conduction is the total thermal conductivity, written as κ_{total}. Figure 7(c)−Figure 9(c) show the estimated electronic (hole) thermal conductivity $\kappa_e(T, e(h))$. The electronic thermal conductivity κ_e is related to the electronic conductivity σ by the Wiedemann−Franz law: $\kappa_e = L\sigma T$, where L is the Lorentz number. The electronic thermal conductivity and electronic conductivity follow a similar pattern. Figure 7(c) indicates that changes in temperature and the doping carrier concentration of e(h) affect electronic thermal conductivity. It is shown that in comparison to increases in e(h) doping concentrations, $\kappa_e(T, e))$ climbs quicker with increasing for n-type doped CrS_2 monolayers, so the $\kappa_e(T, e)$ increases at a substantially higher pace than the $\kappa_h(T, h)$, resulting in a high figure-of-merit ZT value. A similar trend is followed by Janus CrSTe and pristine $CrTe_2$ monolayers, as shown in Figure 8(c) and Figure 9(c), respectively.

It has been observed that the increase in $\kappa_h(T, h)$ is slower as compared to $\kappa_e(T, e)$ for $CrS_{2-x}Te_x$ monolayers. This results in high ZT values for hole-doped $CrS_{2-x}Te_x$ monolayers. ZT is the determining factor for the efficiency of a material in thermoelectricity. Experimental reports show that the semiconducting p-type MoS_2 monolayers have a ZT value of 0.18 at T = 1000 K, obtained by embedding VMo_2S_4 nanoinclusions in MoS_2 monolayer.[59] Despite having a very small electronic thermal conductivity,[60] it is still a good conductor. In determining the values of $ZT = \frac{\sigma S^2 T}{\kappa_e + \kappa_{lat}}$, clearly in the denominator both κ_e and κ_{lat} are added together. So, we treat the value of κ_{lat} is a constant parameter at constant temperature and varying the value of κ_e is a function of electron and hole doping concentration.

Figures 7(d) and 9(d) present ZT at various temperatures and varying e(h)-doping concentrations. It can be seen that in our current study, the highest ZT value for CrS_2 monolayer is calculated as 0.02 at room temperature, while ZT = 0.09 at 500 K. Figure 8(d) shows that at doping concentration 2.0×10^{119} cm^{-3}, ZT is computed 0.01 for electron-doped Janus CrSTe

https://doi.org/10.1021/acsomega.4c01767
ACS Omega 2024, 9, 23782−23792

monolayer, smaller by amount 0.05 than the figure-of-merit estimated for hole-doped CrS_2 monolayer. At the particular (optimal) doping concentration, we demonstrated that the figure-of-merit increases with an increase in temperature and decreases with an increase in the e(h)-type dopant concentration. The above observations suggest that thermoelectric devices operated at high temperatures may utilize $CrS_{2-x}Te_x$ monolayers. High ZT values can be achieved in monolayer compounds of $CrS_{2-x}Te_x$ by inclusion of p-type doping concentrations. These compounds exhibit better thermoelectric performance when compared to n-type doping concentrations. The improved performance is due to the heavy hole's large effective mass and low hole thermal conductivity.

4. CONCLUSION

In the present study, the structural, phonon spectrum, elastic, electronic, and thermal transport properties of CrS_2, Janus CrSTe, and $CrTe_2$ dichalcogenides monolayers are systematically investigated using first-principles calculations together with semiclassical Boltzmann transport theory. The negative formation energy, phonon spectrum, and elastic constants demonstrate that CrS_2, Janus CrSTe, and $CrTe_2$ possess structural stability, dynamic stability, and high mechanical stability, which in turn realize the feasibility of the synthesis of these monolayers in the experiment. The pristine CrS_2 and $CrTe_2$ monolayers are semiconductors with GGA+PBE calculated direct bandgap (K−K) of 1.01 and 0.67 eV, respectively. The Janus CrSTe monolayer is a semiconductor with a small indirect bandgap of 0.31 eV (Γ−K). Due to the strong anharmonic scattering, at higher temperatures, low lattice thermal conductivity is calculated for CrS_2, CrSTe, and $CrTe_2$ monolayers with values 2.09 0.99, and 0.80 W/mK, respectively. This will imply excellent thermoelectric performance. Comparisons are made between pristine CrS_2, $CrTe_2$, and Janus CrSTe monolayers. The CrS_2 and $CrTe_2$ monolayers follow nearly identical trends in thermoelectric parameters as the temperature and e(h)-doping concentrations increased. In contrast, the electrical conductivity enhanced while electronic thermal conductivity decreased. The calculated $S(T, \mathrm{h})$ is larger than the $S(T, \mathrm{e})$ of the CrS_2 monolayer at any temperature and doping concentration value. At 500 K, the e(h)-doped $CrTe_2$ has a ZT value of around 0.09 (0.05), indicating that it has an efficient n(p)-type thermoelectric performance and can be considered a potential candidate for thermoelectric applications. The ZT for the $CrS_{2-x}Te_x$ monolayer slightly decreased with an increasing temperature at fixed concentrations. According to our calculations, $CrS_{2-x}Te_x$ might be employed in thermoelectricity generation at high temperatures for thermopower generation and highly effective waste heat recovery. Our findings would provide not only a basic understanding of electronic and thermoelectric characteristics of $CrS_{2-x}Te_x$ monolayers but also fresh recommendations for the experimental investigations of $CrS_{2-x}Te_x$ monolayers.

AUTHOR INFORMATION

Corresponding Authors

Bao Jingfu − *School of Integrated Circuit Science and Engineering, University of Electronic Sciences and Technology of China, Chengdu 610054, People's Republic of China*; Email: baojingfu@uestc.edu.cn

M. Abdul − *School of Integrated Circuit Science and Engineering, University of Electronic Sciences and Technology of China, Chengdu 610054, People's Republic of China*; Email: mabdul@mail.ustc.edu.cn

Altaf Ur Rahman − *Department of Physics, Riphah International University, Lahore 54000, Pakistan*; orcid.org/0000-0001-7772-3272; Email: altaf.urrahman@riphah.edu.pk

Authors

Farva Tufail − *School of Integrated Circuit Science and Engineering, University of Electronic Sciences and Technology of China, Chengdu 610054, People's Republic of China; Department of Physics, Riphah International University, Lahore 54000, Pakistan*

Abdull Farooq − *Department of Physics, Riphah International University, Lahore 54000, Pakistan*

Zeinhom M. El-Bahy − *Department of Chemistry, Faculty of Science, Al-Azhar University, Nasr City 11884 Cairo, Egypt*

Gaber A. M. Mersal − *Department of Chemistry, College of Science, Taif University, Taif 21944, Saudi Arabia*

Muhammad Nisar − *Departamento de Ingeniería Eléctrica, Facultad de Ingeniería, Universidad Católica de la Santísima Concepción, 2850 Concepción, Chile; Universidad Católica de la Santísima Concepción, Centro de Energía, 2850 Concepción, Chile*

Complete contact information is available at: https://pubs.acs.org/10.1021/acsomega.4c01767

Notes

The authors declare no competing financial interest.

ACKNOWLEDGMENTS

The authors extend their appreciation to Taif University, Saudi Arabia for supporting this work through project number (TU-DSPP-2024-21). This work was supported in part by Oracle Cloud credits and related resources provided by the Oracle for Research program (Award Number CPQ-2652238). We acknowledge the Super-Computing facility at Ghulam Ishaq Khan Institute of Engineering Sciences and Technology funded by the Directorate of Science and Technology (DoST), Government of Khyber Pakhtunkhwa, and National Center for Physics (NCP) Islamabad, Pakistan. We gratefully acknowledge the financial support provided by the research project under grant (A1098531023601318), as well as the National Natural Science Foundation of China grant and the China Academy of Engineering Physics under grant (U1430102). M.N. acknowledge Proyecto Ingeniería 2030 (ING222010004).

REFERENCES

(1) Chen, W.; Pöhls, J.-H.; Hautier, G.; Broberg, D.; Bajaj, S.; Aydemir, U.; Gibbs, Z. M.; Zhu, H.; Asta, M.; Snyder, G. J.; et al. Understanding thermoelectric properties from high-throughput calculations: trends, insights, and comparisons with experiment. *Journal of Materials Chemistry C* **2016**, *4*, 4414−4426.

(2) Ullah, H.; Ur Rahman, A.; Leonetti Aragao, E.; Frois Alves Barbosa, F.; Gabriel Ramisch Pergher, K.; Giulian, R.; Coelho Junior, H.; Luis Sommer, R.; Khan, S. Homogeneous V incorporation via single-step anodization: Structural doping or heterostructure formation? *Appl. Surf. Sci.* **2021**, *556*, 149694.

(3) Casian, A.; Sanduleac, I. Thermoelectric properties of tetrathiotetracene iodide crystals: modeling and experiment. *J. Electron. Mater.* **2014**, *43*, 3740−3745.

(4) Ur Rahman, A.; Aurangzeb, M.; Khan, R.; Zhang, Q.; Dahshan, A. Predicted double perovskite material Ca2ZrTiO6 with enhanced n-

type thermoelectric performance. *J. Solid State Chem.* **2022**, *305*, 122661.
(5) Wickramaratne, D.; Zahid, F.; Lake, R. K. Electronic and thermoelectric properties of few-layer transition metal dichalcogenides. *J. Chem. Phys.* **2014**, *140*, 124710.
(6) Rahman, A. U.; Morbec, J. M.; Rahman, G.; Kratzer, P. Commensurate versus incommensurate heterostructures of group-III monochalcogenides. *Physical Review Materials* **2018**, *2*, 094002.
(7) Morales-Ferreiro, J.; Diaz-Droguett, D. E.; Celentano, D.; Luo, T. First-principles calculations of thermoelectric properties of IV−VI chalcogenides 2D materials. *Front. Mech. Eng.* **2017**, *3*, 15.
(8) Zhang, J.; Dong, P.; Dang, K.; Zhang, Y.; Yan, Q.; Xiang, H.; Su, J.; Liu, Z.; Si, M.; Gao, J.; et al. Ultra-wide bandgap semiconductor Ga2O3 power diodes. *Nat. Commun.* **2022**, *13*, 3900.
(9) Terki, R.; Feraoun, H.; Bertrand, G.; Aourag, H. Full potential calculation of structural, elastic and electronic properties of BaZrO3 and SrZrO3. *Physica status solidi (b)* **2005**, *242*, 1054−1062.
(10) Dong-ping, M.; Xi-te, Z.; Zheng-gang, Z.; Yi-sun, X.; Gu-bo, L. The Improved Murnaghan Equation. *Commun. Theor. Phys.* **1988**, *9*, 9.
(11) Flocken, J.; Mo, Z.; Hardy, J.; Lu, H. Diffusive phase transitions in mixed halide ferroelectrics. *Ferroelectrics* **1992**, *136*, 125−136.
(12) Murphy, D. W.; Sunshine, S.; Van Dover, R. B.; Cava, R. J.; Batlogg, B.; Zahurak, S.; Schneemeyer, L. New superconducting cuprate perovskites. *Physical review letters* **1987**, *58*, 1888.
(13) Snyder, G. J.; Toberer, E. S. Complex Thermoelectric Materials. *Materials for Sustainable Energy* **2010**, 101−110.
(14) Levi, B. G. Simple compound manifests record-high thermoelectric performance. *Phys. Today* **2014**, *67*, 14.
(15) Zhang, X.; Zhao, L.-D. Thermoelectric materials: Energy conversion between heat and electricity. *Journal of Materiomics* **2015**, *1*, 92−105.
(16) LaLonde, A. D.; Pei, Y.; Wang, H.; Snyder, G. J. Lead telluride alloy thermoelectrics. *Mater. Today* **2011**, *14*, 526−532.
(17) Mehdizadeh Dehkordi, A.; Zebarjadi, M.; He, J.; Tritt, T. M. Thermoelectric power factor: Enhancement mechanisms and strategies for higher performance thermoelectric materials. *Mater. Sci. Eng., R* **2015**, *97*, 1−22.
(18) Goldsmid, H. J. *Introduction to thermoelectricity*; "Springer Series in Materials Science" series; Springer, 2010; Series Vol. *121*.
(19) Zhang, Y.; Chen, Z.; Zhang, K.; Feng, Z.; Zhao, H. Laser-Assisted Metal−Organic Chemical Vapor Deposition of Gallium Nitride. *Phys. Status Solidi RRL* **2021**, *15*, 2100202.
(20) Guo, S.-D.; Li, Y.-F.; Guo, X.-S. Predicted Janus monolayer ZrSSe with enhanced n-type thermoelectric properties compared with monolayer ZrS2. *Comput. Mater. Sci.* **2019**, *161*, 16−23.
(21) Zhang, G.; Zhang, Y.-W. Thermoelectric properties of two-dimensional transition metal dichalcogenides. *Journal of Materials Chemistry C* **2017**, *5*, 7684−7698.
(22) Guo, H.; Yang, T.; Tao, P.; Wang, Y.; Zhang, Z. High pressure effect on structure, electronic structure, and thermoelectric properties of MoS2. *J. Appl. Phys.* **2013**, *113*, 013709.
(23) Huang, W.; Luo, X.; Gan, C. K.; Quek, S. Y.; Liang, G. Theoretical study of thermoelectric properties of few-layer MoS 2 and WSe 2. *Phys. Chem. Chem. Phys.* **2014**, *16*, 10866−10874.
(24) Zhao, S.; Wang, H. An integrated H-type method to measure thermoelectric properties of two-dimensional materials. *ES Energy Environ.* **2020**, *9*, 59−66.
(25) Wei, J.; Yang, L.; Ma, Z.; Song, P.; Zhang, M.; Ma, J.; Yang, F.; Wang, X. Review of current high-ZT thermoelectric materials. *J. Mater. Sci.* **2020**, *55*, 12642−12704.
(26) Wu, Z.; Zhang, S.; Liu, Z.; Lu, C.; Hu, Z. Bottom-Up (Cu, Ag, Au)/Al2O3/Bi2Te3 Assembled Thermoelectric Heterostructures. *Micromachines* **2021**, *12*, 480.
(27) Wu, Z.; Chen, X.; Mu, E.; Liu, Y.; Che, Z.; Dun, C.; Sun, F.; Wang, X.; Zhang, Y.; Hu, Z. Lattice strain enhances thermoelectric properties in Sb2Te3/Te heterostructure. *Adv. Electron. Mater.* **2020**, *6*, 1900735.
(28) Kohn, W.; Sham, L. J. Self-consistent equations including exchange and correlation effects. *Physical review* **1965**, *140*, A1133.
(29) Giannozzi, P.; Baroni, S.; Bonini, N.; Calandra, M.; Car, R.; Cavazzoni, C.; Ceresoli, D.; Chiarotti, G. L.; Cococcioni, M.; Dabo, I.; et al. QUANTUM ESPRESSO: a modular and open-source software project for quantum simulations of materials. *J. Phys.: Condens. Matter* **2009**, *21*, 395502.
(30) Perdew, J. P.; Burke, K.; Ernzerhof, M. Generalized gradient approximation made simple. *Physical review letters* **1996**, *77*, 3865.
(31) Rappe, A. M.; Rabe, K. M.; Kaxiras, E.; Joannopoulos, J. Erratum: Optimized pseudopotentials [phys. rev. b 41, 1227 (1990)]. *Phys. Rev. B* **1991**, *44*, 13175.
(32) Monkhorst, H. J.; Pack, J. D. Special points for Brillouin-zone integrations. *Phys. Rev. B* **1976**, *13*, 5188.
(33) Guo, G.; Wang, H. Calculated elastic constants and electronic and magnetic properties of bcc, fcc, and hcp Cr crystals and thin films. *Phys. Rev. B* **2000**, *62*, 5136.
(34) Donohue, J.; Caron, A.; Goldish, E. The crystal and molecular structure of S6 (Sulfur-6). *Journal of The American Chemical Society* **1961**, *83*, 3748−3751.
(35) Li, X.-H.; Cui, X.-H.; Xing, C.-H.; Cui, H.-L.; Zhang, R.-Z. Strain-tunable electronic and optical properties of Zr2CO2MXene and MoSe2 van der Waals heterojunction: A first principles calculation. *Appl. Surf. Sci.* **2021**, *548*, 149249.
(36) Rahman, A. U. Strain Induces Ferromagnetism in a Janus Transition Metal Dichalcogenides: CrSTe-1H Monolayer. *J. Electron. Mater.* **2023**, *52*, 1036−1049.
(37) Gandi, A. N.; Alshareef, H. N.; Schwingenschlögl, U. Thermoelectric performance of the mxenes M2Co2 (M= Ti, Zr, or Hf). *Chem. Mater.* **2016**, *28*, 1647−1652.
(38) Tyuterev, V.; Vast, N. Murnaghan's equation of state for the electronic ground state energy. *Computational materials science* **2006**, *38*, 350−353.
(39) Zhuang, H. L.; Johannes, M. D.; Blonsky, M. N.; Hennig, R. G. Computational prediction and characterization of single-layer CrS2. *Appl. Phys. Lett.* **2014**, *104*, 022116.
(40) Cui, Q.; Liang, J.; Shao, Z.; Cui, P.; Yang, H. Strain-tunable ferromagnetism and chiral spin textures in two-dimensional Janus chromium dichalcogenides. *Phys. Rev. B* **2020**, *102*, 094425.
(41) Rahman, A. U.; Ali, S.; Awan, A. A.; Hayat, S.; Dahshan, A.; Rahman, G. Investigation of room-temperature ferromagnetism in perovskite structure via substitutional doping. *Eur. Phys. J. Plus* **2021**, *136*, 1137.
(42) Khazaei, M.; Arai, M.; Sasaki, T.; Chung, C.-Y.; Venkataramanan, N. S.; Estili, M.; Sakka, Y.; Kawazoe, Y. Novel electronic and magnetic properties of two-dimensional transition metal carbides and nitrides. *Adv. Funct. Mater.* **2013**, *23*, 2185−2192.
(43) Togo, A. First-principles phonon calculations with phonopy and phono3py. *J. Phys. Soc. Jpn.* **2023**, *92*, 012001.
(44) Togo, A.; Chaput, L.; Tadano, T.; Tanaka, I. Implementation strategies in phonopy and phono3py. *J. Phys.: Condens. Matter* **2023**, *35*, 353001.
(45) Zhao, P.; Liang, Y.; Ma, Y.; Huang, B.; Dai, Y. Janus chromium dichalcogenide monolayers with low carrier recombination for photocatalytic overall water-splitting under infrared light. *J. Phys. Chem. C* **2019**, *123*, 4186−4192.
(46) Chaves, A.; Azadani, J. G.; Alsalman, H.; Da Costa, D.; Frisenda, R.; Chaves, A.; Song, S. H.; Kim, Y. D.; He, D.; Zhou, J.; et al. Bandgap engineering of two-dimensional semiconductor materials. *npj 2D Mater. Appl.* **2020**, *4*, 29.
(47) Rahman, A. U.; Ullah, H.; Jamil, A.; Iqbal, Z.; Naveed-Ul-Haq, M. Robust ferromagnetism and half-metallicity in hydrogenated monolayer-CdS. *Physica B: Condensed Matter* **2019**, *570*, 209−216.
(48) Sevinçli, H.; Cuniberti, G. Enhanced thermoelectric figure of merit in edge-disordered zigzag graphene nanoribbons. *Phys. Rev. B* **2010**, *81*, 113401.
(49) Rahman, G.; Rahman, A. U. Thermoelectric properties of n and p-type cubic and tetragonal XTiO3 (X= Ba, Pb): A density functional theory study. *Physica B: Condensed Matter* **2017**, *526*, 122−126.

https://doi.org/10.1021/acsomega.4c01767
ACS Omega 2024, 9, 23782−23792

(50) Rahman, A. U.; Jamil, A.; Khan, S.; Ibrar, M.; Ullah, I.; Ahmad, R.; Dahshan, A. First-Principles Computational Exploration of Thermoelectric Properties of Bulk-GaN and Monolayer-GaN. *J. Electron. Mater.* **2022**, *51*, 3317−3328.
(51) Tufail, M.; Rahman, A. U.; Gul, B.; Akram, W.; Ullah, H.; Iqbal, M. W.; Ramay, S. M.; Shah, W. H. Effect of Pb doping on electronic and thermoelectric properties of thallium antimony telluride (Tl8. 33Sb1. 67- xPbxTe6) nano-compound: a combined experimental and theoretical investigations. *Physica B: Condensed Matter* **2021**, *608*, 412789.
(52) Sun, J.; Singh, D. J. Thermoelectric properties of n-type SrTiO3. *APL Mater.* **2016**, *4*, 104803.
(53) Rahman, J. U.; Nam, W. H.; Van Du, N.; Rahman, G.; Rahman, A. U.; Shin, W. H.; Seo, W.-S.; Kim, M. H.; Lee, S. Oxygen vacancy revived phonon-glass electron-crystal in SrTiO3. *Journal of the European Ceramic Society* **2019**, *39*, 358−365.
(54) Khan, W. M.; Rahman, A. U.; Tufail, M.; Ibrar, M.; Shah, W. H.; Syed, W. A.; Gul, B. Toward controlled thermoelectric properties of Pb and Sb co-doped nanostructured Thallium Telluride for energy applications. *Materials Research Express* **2020**, *7*, 105010.
(55) Madsen, G. K.; Singh, D. J. BoltzTraP. A code for calculating band-structure dependent quantities. *Comput. Phys. Commun.* **2006**, *175*, 67−71.
(56) Awasthi, C.; Islam, S. Excellent Seebeck coefficient observed in exfoliated N-type Tungsten Disulphide (WS2). *Materials Science in Semiconductor Processing* **2023**, *162*, 107554.
(57) Ding, G.; Gao, G.; Huang, Z.; Zhang, W.; Yao, K. Thermoelectric properties of monolayer MSe2 (M= Zr, Hf): low lattice thermal conductivity and a promising figure of merit. *Nanotechnology* **2016**, *27*, 375703.
(58) Hippalgaonkar, K.; Wang, Y.; Ye, Y.; Qiu, D. Y.; Zhu, H.; Wang, Y.; Moore, J.; Louie, S. G.; Zhang, X. High thermoelectric power factor in two-dimensional crystals of Mo S 2. *Phys. Rev. B* **2017**, *95*, 115407.
(59) Kong, S.; Wu, T.; Zhuang, W.; Jiang, P.; Bao, X. Realizing p-type MoS2 with enhanced thermoelectric performance by embedding VMo2S4 nanoinclusions. *J. Phys. Chem. B* **2018**, *122*, 713−720.
(60) Feng, K.; Xu, L.; Xiong, Y.; Sun, L.; Yu, H.; Wu, M.; Thant, A. A.; Hu, B. PEDOT: PSS and Ni-based thermoelectric generator for solar thermal energy conversion. *Journal of Materials Chemistry C* **2020**, *8*, 3914−3922.

https://doi.org/10.1021/acsomega.4c01767
ACS Omega 2024, 9, 23782−23792